Estimating Fuel Moisture in Grasslands Using UAV-Mounted Infrared and Visible Light Sensors

Nastassia Barber

A dissertation

submitted in partial fulfillment of the

requirements for the degree of

Master of Science

University of Washington

2021

Reading Committee:

Ernesto Alvarado, Chair

Van Kane

William Mell

Monika Moskal

Program Authorized to Offer Degree:

School of Environmental and Forest Sciences

University of Washington

Abstract

Estimating Fuel Moisture in Grasslands Using UAV-Mounted Infrared and Visible Light Sensors

Nastassia Barber

Chair of the Supervisory Committee:
Ernesto Alvarado, Research Associate Professor
School of Environmental and Forest Sciences

Predicting wildfire behavior is a complex task which has historically relied on empirical models. Physics-based fire models could potentially improve predictions and have wide applicability, but these models require more detailed inputs, including spatially explicit estimates of fuel characteristics. One of the most critical of these characteristics is fuel moisture. Obtaining moisture measurements with traditional destructive sampling techniques can be prohibitively time-consuming and extremely limited in resolution. This study seeks to assess how effectively moisture in grasses can be estimated using reflectance in six wavelengths in the visible and infrared ranges. We collected 120 1 m-square field samples in a western Washington grassland and collected overhead imagery in six wavelengths for the same area. Predictive models of vegetation moisture using existing vegetation indices as well as components from principal component analysis of the wavelengths were generated and compared. The best model, a linear model based on principal

components and biomass, showed modest predictive power (r^2=.45). This model performed better for the plots with both dominant grass species pooled than it did for each individually. Given the limited scope of this study especially regarding moisture range, the presence of this correlation suggests that further research using samples across the entire fire season could potentially produce effective models for estimating moisture in this type of ecosystem using UAVs, even when more than one major species of grass is present. This approach would be a fast and flexible approach compared to traditional moisture measurements.

TABLE OF CONTENTS

LIST OF FIGURES

LIST OF TABLES

ACKNOWLEDGEMENTS

This research was funded by a Joint Venture Agreement 19-JV-11261987-139 with the USFS PNW Research Station "Integration of New Generation of 3-D Fuel Characterization, Physics-Based Fire Models, and Tree Mortality".

Thank you to my committee, Dr. Ernesto Alvarado (chair), Dr. William Mell, Dr. Monika L. Moskal, and Dr. Van Kane for providing me with assistance and advice throughout the process.

Thank you to the Autonomous Systems Flight Laboratory at UW for providing equipment and guidance as well as assistance with field work. Thank you to the USFS for providing use of both the lab and the test site. Both of these organizations were also extremely helpful in managing field work schedules and developing ways to comply with Covid-19 guidelines.

Many thanks to Liz vanWagtendonk, Harry Podschwit, and other members of the Pacific Fire Sciences Laboratory and Remote Sensing and Geospatial Analysis Laboratory for advice and support. Thanks to Derek McNamara and Jim Cronan from the Forest Service for their expertise.

Huge thank you to Westy, Rikki, Eva, Spencer, and Guy for providing logistical and other support throughout this research.

Chapter 1. INTRODUCTION

Existing research on wildfire behavior is vast and has a broad range of motivations, including biodiversity concerns, carbon sequestration, health risks posed by smoke, and danger to homes in the Wildland Urban Interface (WUI). Fires are both an important part of forest health and a major danger to people and the environment, but fire behavior and risk is challenging to predict partly because both environmental conditions and development of fire-prone landscapes have been changing so rapidly in recent decades. The prevalence and severity of fires has measurably increased since 1960 due to increasing average temperatures, severe winds, and land use changes [1–3]. In addition, the number of homes in the WUI is increasing, and many of them are in these areas with fire severity that exceeds the historical norms. This increase provides significant motivation for further study of fire behavior, especially in the ecosystems with increased WUI development [4,5]. In addition to determining the risk to homeowners, an understanding of fire behavior and the factors that contribute to ignition is desirable in order to better inform management decisions such as prescribed burning or thinning to reduce risk [6–8].

It is not only temperature increases, but also decreases in relative humidity, that contribute to these changes in fire frequency and severity [9]. Local fuel moisture can be prohibitively expensive and difficult to measure, as traditionally it has been measured by destructively sampling the vegetation, followed by a lengthy drying process [10]. More broadscale mapping of fuel moisture is possible based on weather information. Because moisture is an important factor in predicting fire risk and behavior, it is necessary for informed land management decision-making [11–14]. The importance of accurately measuring fuel moisture only increases as climate change becomes a dominant factor in fire behavior and as models are developed that make predictions based on fluid dynamics.

Two technological developments have the potential to increase the ease and accuracy with which fire behavior can be predicted and methods to reduce risk can be evaluated. One of these is the increased availability of computational resources. This includes both processing software/techniques and computational power [15]. The other is the increased availability of aerial imagery-- whether from satellite data, airplanes, or UAVs, which are becoming increasingly affordable, user-friendly, and ubiquitous. UAVs are now available to even small research organizations and hobbyists [16,17]. These two developments together make it possible to create models more informed by data, notably moisture data.

Historically, fire models have been empirical or semi-empirical models that do not directly attempt to simulate the physics that drive fire behavior. Examples of these models include the Rothermel model [18] and the Balbi model [19]. With improved processing power, the WFDS model based on modeling fire physics is being developed to better understand fire behavior and ultimately inform and improve the performance of empirical models. Another potential benefit is that a physics-based model could be used to predict fire behavior in complex situations, such as WUI areas with a combination of roads, vegetation and buildings as opposed to the relatively uniform vegetation cover which is assumed by most models [5]. WFDS is different from most existing models in that it integrates fuel conditions, atmospheric effects, and fire physics into a model of the physical processes at work [20]. In order to validate the WFDS model with regards to moisture inputs, processes must be developed to create spatially-explicit moisture measurements for model validation efforts. A simple ecosystem with which to develop these processes is grasslands.

Reflectance data in a variety of wavelengths has shown promise in detecting vegetation moisture. Chlorophyll is a strong absorber of many infrared wavelengths and red and a weak absorber of green and blue light. Generally, these effects are more pronounced in healthier, greener, more moist vegetation [21,22]. Much research has been done using imagery from satellites such as MODIS [23–25] or Landsat or from other airborne sensors such as AVIRIS or UAV-mounted sensors [26,27]. Some research has shown short wave infrared (SWIR) is also a good predictor of vegetation moisture [28–30], but in some ecosystem types an index based on visible wavelengths alone (VARI) performs better [31,32]. With so many sensor options, large differences in model performance between ecosystems, and a broad range of prices, it is important to determine for a given ecosystem which techniques work best.

Comparatively few studies exist which measure the moisture of non-agricultural vegetation using UAV imagery. This study seeks to explore the use of two different infrared cameras along with visible wavelengths for providing high-resolution fuel moisture inputs for the WFDS model. The potential of this method will be evaluated by using traditional field measurements as a "ground truth" and building a predictive model based on reflectance values in six wavelength bands. In this way, recommendations can be made for future research in live fuel moisture estimation.

1.1 FIRE BEHAVIOR AND MOISTURE

Fire models, from the Rothermel model [18] to more modern models such as WFDS, have been developed to characterize wildfire behavior given inputs about weather conditions, fuel types, fuel characteristics, etc. [33]. These models are useful for managers making decisions about resource allocation or preventative measures for wildfires.

Most if not all major fire modeling tools use fuel moisture as an input. Moisture is a critical part of fire modeling because it is one of the fuel attributes that most contributes to both likelihood of ignition and fire behavior. In some environments, such as Mediterranean shrublands, reaching a critical threshold of moisture can be a good predictor of when a fire is likely to occur [23,34].

1.2 WFDS MODEL

Most models developed to predict fire behavior, chance of ignition, and spread rate are either empirical or semi-empirical. The Wildland-Urban Interface Fire Dynamics Simulator (WFDS) model, an extension of the FDS model created by the National Institute of Standards and Technology, is a physics-based model that aims to improve general understanding of fire-behavior in a more broadly-applicable way than models which rely on very species-specific measurements [35,36]. One motivation for the creation of this model is improving existing models with new physical insights. Another benefit is that a physics-based model could be used to predict fire behavior in complex situations, such as WUI areas with a combination of roads, vegetation and buildings as opposed to the relatively uniform vegetation cover which is assumed by most models [5]. Though still very computationally expensive, WFDS is different from most existing models in that it accounts for fuel conditions, atmospheric effects, and fire physics at the same time [20].

1.3 VEGETATION MOISTURE CHARACTERIZATION

Many models rely on a spatially-explicit quantification of fuel moisture in order to predict fire behavior [37]. Fuel moisture content is usually studied in two separate components- live (LFMC) and dead (DFMC) moisture content. Dead vegetation, such as branches, fallen leaves, and duff, responds more quickly to atmospheric changes, while live fuel responds more to soil moisture and longer-term weather trends [12]. Therefore, it makes sense to model them separately. FMC is calculated in the field by measuring the weight of the fuel immediately and then after oven drying. The result is a percentage given by the following [38]:

$$\text{FMC} = \frac{fresh\ weight - dry\ weight}{dry\ weight} * 100 \qquad (1.1)$$

For the sake of fire modeling and risk assessment, remote sensing methods provide significant advantages. Field measurements are time consuming and only measure a small area. Data collected from satellites or airplanes allow large swaths of land to be measured at once, so that land can be more easily monitored for change over time. Data from UAVs allow for more detailed moisture inputs representing a smaller area, which can provide raster inputs for modeling rather than scattered ground measurements at specific locations.

Most remotely sensed moisture measurements are ratios involving the reflectance of the vegetation in different wavelengths. Sensors equipped to measure various narrow bands of light are used to create images in the visible, ultraviolet, microwave, or infrared parts of the electromagnetic spectrum. These bands all require different interpretations based on the physical mechanism of their absorption/reflectance. Water-stressed plants experience a decrease in chlorophyll, so that these pigment changes may be used to estimate FMC [27]. However, the physical effects that lead to changes in reflectance are different by species and often muddied by internal scattering effects, so it is not always obvious what effect moisture changes will have on the spectral signature of a given plant.

1.4 MEASURING REFLECTANCE IN NARROW BANDS

The set of wavelengths reflected by an object and the intensity of each reflected wavelength is called its spectral signature. Spectral signatures are often used to identify materials or determine their properties. One way to get specific information about the spectral attributes of vegetation is to measure specific wavelengths in relatively narrow bands so that the effects that change the reflectance in a given band can be isolated [39]. Unlike an ordinary camera which is sensitive to a broad range of wavelengths, this study uses six different sensors which are each sensitive to a specific wavelength band. There are many physical effects that contribute to a material's spectral signature, including fluorescence, crystal field effects, and energy transitions in covalent bonds [22]. Chlorophyll, the primary material in grass that reflects light, can undergo several spectral changes when the plant is placed in different soil or water conditions. The specific changes and the sensitivity of the plant to the environment is highly dependent on the species. In this study, the reflectance of the material in each wavelength is used, which is a number between zero and one calculated by comparing the proportion of the light that is reflected compared to an object of known (very high) reflectance.

In addition to the readily available visible light data (red, green and blue bands), various infrared wavelengths have been used to measure vegetation moisture. The most common range is near-infrared, used in the widely used NDVI "greenness" metric. While NIR reflectance is usually found to be inversely related to leaf moisture, this is not universal and some studies have found the opposite effect [26].

While instruments that measure reflectance in the near infrared are more common, it is possible that short wave infrared (SWIR) wavelengths are even more responsive to changes in water content. Water absorbs wavelengths in infrared between about 1.4 and 2 micrometers, so these wavelengths can be "directly" used to measure water content [21,26]. Still, infrared wavelengths, while frequently used in moisture estimations, may be indirectly affected by scattering effects from the plant structure and [27], and also can be more sensitive to atmospheric scattering effects, which poses problems especially when using satellite imagery [40]. SWIR bands from satellite or aerial imagery have been used in many applications to characterize crop or fuel moisture content [41,42].

1.4.1 *NDVI*

Near infrared wavelengths respond to moisture changes, possibly in part due to changes in pigment absorption [43]. However, these wavelengths are also affected by atmospheric changes. Still, NIR sensors are readily available, and as such, NDVI is a common index used in characterizing fuel moisture:

$$\mathrm{NDVI} = \frac{NIR-Red}{NIR+Red} \qquad (1.2)$$

SAVI is a variant of NDVI that attempts to account for soil moisture by including an adjustment factor L based on soil reflectance, which can improve the accuracy, especially in situations with less canopy closure [44].

$$\mathrm{SAVI} = \frac{NIR-Red}{NIR+Red-L} * (1+L) \qquad (1.3)$$

1.4.2 *VARI*

VARI is an index based only on visible light wavelengths. This index has many logistical advantages since visible light sensors are so lightweight, cheap, and readily available. Several studies have found that this is correlated with LMFC in many vegetation types relevant to fire modeling [27]. This is because the green and red bands represent changes in pigment which tend to occur when a plant is water stressed. In addition, though it is not a direct measure of water content, VARI has the advantage of being less affected by atmospheric variables due to the subtraction of the blue term. VARI is given by:

$$\text{VARI} = \frac{Green-Red}{Green+Red-Blue} \qquad (1.4)$$

1.4.3 *NDWI*

Wavelengths in the SWIR range (0.7 to 1.3 μm) are extremely responsive to water content because the refractive index of the leaf cell is largely determined by moisture, but they are also affected by other internal scattering effects, which means they are influenced as well by the geometry and structure of the vegetation. SWIR alone provides a better measurement of Equivalent Water Thickness (EWT) rather than directly measuring FMC [28]. For this reason, an index including both NIR and SWIR bands was developed in an effort to account for this effect, since the scattering effects in SWIR and NIR are similar. This index is called the normalized difference water index:

$$\text{NDWI} = \frac{NIR-SWIR}{NIR+SWIR} \quad (1.5)$$

This index is less sensitive to atmospheric changes than NDVI, but does not eliminate the effects of soil moisture [45].

1.5 UAV DATA COLLECTION

Ideally, a system would be developed for managers to measure fuel moisture using remote sensing to avoid time-consuming and limited field measurement procedures and to be able to predict fire behavior more reliably and efficiently over larger areas than point-based physical sampling methods. This system would consist of i) a platform with which to carry the sensors over the landscape, ii) sensors that record wavelengths that are correlated with fuel moisture, and iii) a processing workflow to obtain moisture estimates from this data.

Regarding the first requirement, remote sensing imagery can be collected via satellite, airplane, or small UAVs. The advantages of UAVs include lower cost and higher-resolution imagery and ready availability. A study can more easily be repeated multiple times in a season with a drone than with an airplane, where each flight is logistically prohibitive. While monitoring of larger areas is best done with satellite data, it is not reasonable to use this data for changes over relatively small geographical areas or short amounts of time. For these reasons, UAVs are a good vehicle both for this study and for some potential future applications of this technology.

Chapter 2. MATERIALS AND METHODS

2.1 SITE SELECTION

The study area was in western Washington, USA at the Center for Natural Lands Management (CNLM) Mazama Meadows land holding in Rochester, WA. The area included 120 plots, each 1m x 1m, arranged in a grid. Sixty of the plots were on each side of a dirt road. The vegetation on one side was taller and primarily consisted of tall oat grass (*Arrhenatherum elatius*) while the vegetation on the other side was more mixed, including the oat grass as well as other grasses including *Agrostis stolonifera*. These two types of vegetation are referred to as “tall” and “short” below. Both vegetation types included a small amount of scotch broom (*Cytisus scoparius*), which was expected to have a far higher water content than the grass fuels.

The fuels ranged in height from approximately 0.1 m to 1.5 m. The site was chosen because it was free of trees or other obstacles that could create shadows, dominated by grass species that exist in a fire prone WUI area, and relatively flat and uniform to avoid effects from topography.

For moisture data, timing is also critical. A highly accessible site was chosen to allow for development of the data collection process over the course of the season, instead of in one long visit to a remote area. The site also has many sunny days in the summer, which enabled all flights and field measurements to be performed as close as possible to solar noon and in direct sunlight. This was necessary to create consistent lighting conditions for comparison between flights.

Figure 2.1. Overhead Image of Study Site

Error! Reference source not found. shows the study site in context, with visibly different types of vegetation on either side of the primitive road.

2.2 IMAGERY DATA COLLECTION

The data was collected using a FLIR Tau SWIR camera and the Micasense RedEdge multispectral camera mounted to a DJI M600 drone. The Tau is a specialized video camera that records video in a single, short-wave infrared band. It was equipped with a 25mm lens. The Micasense is a five-band camera that records separate images in the red, green, blue, red edge, and near-infrared bands. The Micasense is a product designed for non-engineers and is comparatively inexpensive and easy to use. The Tau was controlled and powered by an onboard Raspberry Pi, and the Micasense was controlled by a mobile app over its WiFi network. Both the Micasense and the Raspberry Pi were powered using battery packs mounted to the drone.

A resolution of 5cm or less was desirable to ensure that the variation within each plot was captured. The following formulas were used to determine the horizontal and vertical angle of view (AOV) and coverage (C) of the camera, where p is the sensor size in that dimension, d is the distance of the camera from the subject and f is the focal length [46].

$$\mathrm{AOV} = 2 * \arctan\left(\frac{p}{2f}\right) \qquad (2.1)$$

$$\mathrm{C} = 2 * \mathrm{d} * \tan\left(\frac{AOV}{2}\right) \qquad (2.2)$$

The Tau camera, which was the limiting factor for both resolution and coverage, has a 9.6 x 7.68 mm sensor; so with a 25 mm lens and a typical flight height of 16m, this gave a coverage of 6.1 m horizontally and 4.6 m vertically. This corresponds to a resolution of 1.1 cm. UgCS was chosen as the flight control software due to its ability to set specific ground speed and elevation for repeatable flights. UgCS also includes functionality to determine image overlap in flight planning. Though there is some variation among previous studies, a frequent target for front overlap is 60-85% or higher and side overlap was 40-85%. In this study the side and front overlap were both set to 85% based on Micasense parameters to improve alignment in preprocessing [42,47,48]. These parameters were successful at producing images with 85%+ overlap for the Micasense images, but the side overlap was less for the Tau images. Each image was taken at a 16m height and at a speed of 3 m/s. A double-grid pattern was used to ensure proper coverage of the study area. Each flight took approximately ten minutes.

Foam pool noodles and metal objects were placed around the study area so that they would be visible from above and aid in image alignment as shown in Figure 2.2. The drone was also flown over the Micasense calibrated reflectance panel to obtain calibration data for known reflectance values.

The specific wavelengths recorded in the study are shown in

Table 2.1.

Table 2.1. Wavelength Bands

Band	Wavelength Range
Blue	475 +/- 16 nm
Green	560 +/- 13.5 nm
Red	668 +/- 7 nm
Red Edge	717 +/- 6 nm
NIR	842 +/- 28 nm
SWIR	1050 +/- 200 nm

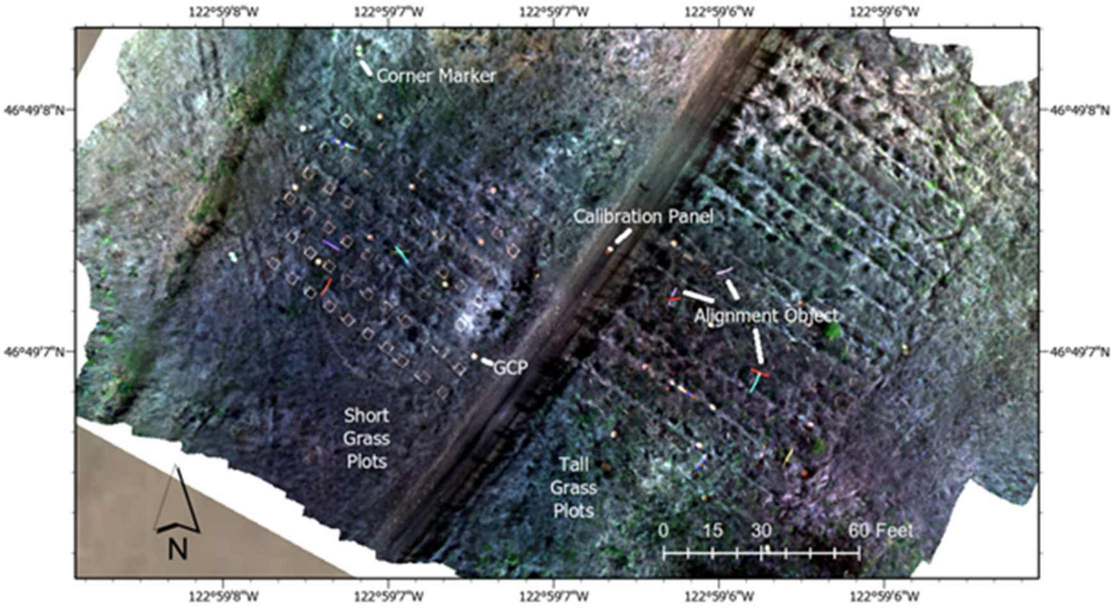

Figure 2.2. Layout of Study Site

2.3 FIELD DATA COLLECTION

Field measurements were collected by destructively sampling plots, placing the vegetation in a sealed plastic bag, and weighing the samples before and after 48 hours of oven drying at 70 degrees Celsius. Each plot was marked by a square of PVC pipe and a vertical pipe labeled with the plot number. The vertical pipe made it much easier to locate the plots in the tall grass in overhead imagery, and it also allowed the field crew to find their assigned plots much more quickly. All bags were labeled with the name of the person who collected the sample, the time, the date, and the plot number. All samples were collected within two hours of the flight time, as in previous studies [49,50]. The plots collected after each flight/by each person were selected such that 30 of each grass type were sampled at each time, but the locations of the selected samples were completely randomized within the type.

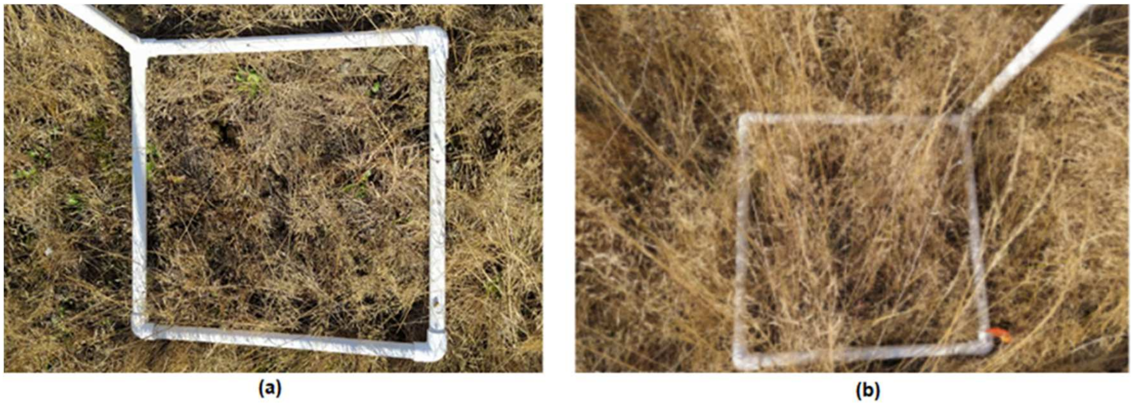
(a) (b)

Figure 2.3. Examples of Plots in Short Grass (a) and Tall Grass (b)

To best represent the vegetation measured in the aerial imagery, as well as the vegetation most critical to fire behavior, each sample was divided into three parts. First, since most of the vegetation was dry grass, the few pieces of brush and other leafy vegetation (mostly scotch broom) were placed in a separate bag. It is unclear if a model, trained on data mostly reflecting the much drier grass, would meaningfully reflect changes in the moisture of the bushes, and they were not very numerous in the study area. This moisture of this subset of the sample is referred to as “green” moisture below.

Then, the grass was separated into fuels 12” or more above the ground (denoted “top” moisture) and fuels below this threshold (denoted “bottom” moisture), using a piece of PVC pipe cut to this length as a reference. This opens up analysis to include either the total moisture or some subset of these vertically segmented parts.

GPS data for the sixteen ground control points located throughout the study area was also collected using a survey-grade GPS unit.

2.4 PRE-PROCESSING METHODS

The Micasense outputs a collection of groups of five images, each representing an individual wavelength. The Tau outputs a video, and I used ffmpeg, a video processing program, both to record the video and to extract frames as images from the recorded video at 8 frames per second.

For each of the six wavelength bands listed in Table 2.1, one large orthoimage covering the study area was created. This stitching operation was performed in Agisoft Metashape using a similar processing workflow as previous studies [51,52]. For the Micasense data, this was accomplished with very few unaligned images and no gaps in the study area. With the Tau data, only a few dozen of the hundreds of images aligned using the default settings. Many could be aligned by separating them into "chunks" which could then be aligned with each other in a later step. Still, the preprocessed Tau data included coverage for only about 80% of the plots. These aligned images were used to create an orthomosaic from a high-quality mesh.

Next, using the reflectance values for the calibration panel used in the field, the stitched images were calibrated to the actual reflectance in each wavelength, using the calibration tool in Metashape. Then, each wavelength was exported as an orthomosaic in .TIFF format (or in the case of the Tau, as several chunks). Next, in ArcGIS Pro, the ground control point coordinates collected in the field were used to locate the false-color image. Then, using georeferencing tools, the rest of the layers were aligned, and the Tau raster was combined into a single raster. The Tau "chunks" were aligned using the alignment objects in the field, and a chunk was rejected and not included in the analysis if it appeared significantly distorted or fewer than 4 alignment objects could be located.

The plot borders were visually located in the false-color image, and a shapefile was created that delineated everything inside the PVC border and as little of the (highly reflective) PVC pipe as possible.

Outliers with very high reflectance were eliminated to remove the influence of the PVC pipe. By observing the values of the pipes and the grass, this was estimated to be values greater than 225 for SWIR, greater than 180 for the other infrared wavelengths, and greater than 140 for the visible wavelengths. (Note that at this point reflectance is still scaled between 0 and 255 instead of 0-1). Then, a table was created with the mean, median, and standard deviation for the reflectance values in each wavelength for each plot. After repeating the above steps for the second flight, a table with the means, medians, and standard deviations for each wavelength (for both sets of flight data) was created and exported.

A MATLAB script was created to generate image homogeneity values for each plot to serve as a second potential texture metric in addition to standard deviation.

The above steps are explained in more detail in Appendix B.

2.5 STATISTICAL ANALYSIS

The statistical analysis was performed in R. First, some preliminary analysis was performed on the field moisture measurements to examine the distribution. A comparison was made between different methods of calculating the moisture for the tall grass using the three subsets of moisture collected—top, bottom, and green. We compared top moisture alone to top and bottom combined and to the total moisture of these components. We also tested the field moisture measurements for spatial effects using a Mantel test comparing two Euclidean distance matrices, one for the moistures of the three subsets of the plot and one for the coordinates of the sample locations on the 1m sampling grid. [53]. No significant spatial effects were found (r=-.04, p=.96), so spatial effects were not accounted for in the analysis.

Then, using the plot mean values for the reflectance data, the vegetation indices mentioned above were calculated by plot. For comparison, we also performed Principal Component Analysis on the reflectance data using the princomp function to create another set of predictive components. PCA uses a linear transformation to generate combinations of the input variables that are linearly uncorrelated with each other but explain as much of the variation in the reflectance data as possible. This provides an alternative way to include multiple wavelengths in the model since the data for the various wavelengths are highly correlated with each other. PCA was performed on the five wavelengths excluding SWIR.

Then, multiple linear models were created to compare the results from vegetation indices to the principal components. Other variables were included as potential covariates: standard deviation in the NIR layer, homogeneity in the NIR layer, the time between the imagery and field data collection, the grass type, and the total weight of the grass at each plot. Models were first created for each of the indices and for principal components using all potential terms, then backwards elimination was used to eliminate parameters until the model was not improved. The metrics used for improvement were the Akaike Information Criterion and the adjusted r^2. For comparison, models were also created for the two vegetation types separately based on the best-performing predictors for the overall models.

Chapter 3. RESULTS

3.1 COMPARISON OF MOISTURE MEASUREMENT METHODS

After removing plots with sampling errors, the final sample size was n=118. The moisture distribution of the field samples is shown in Figure 3.1, for each of the two different vegetation types.

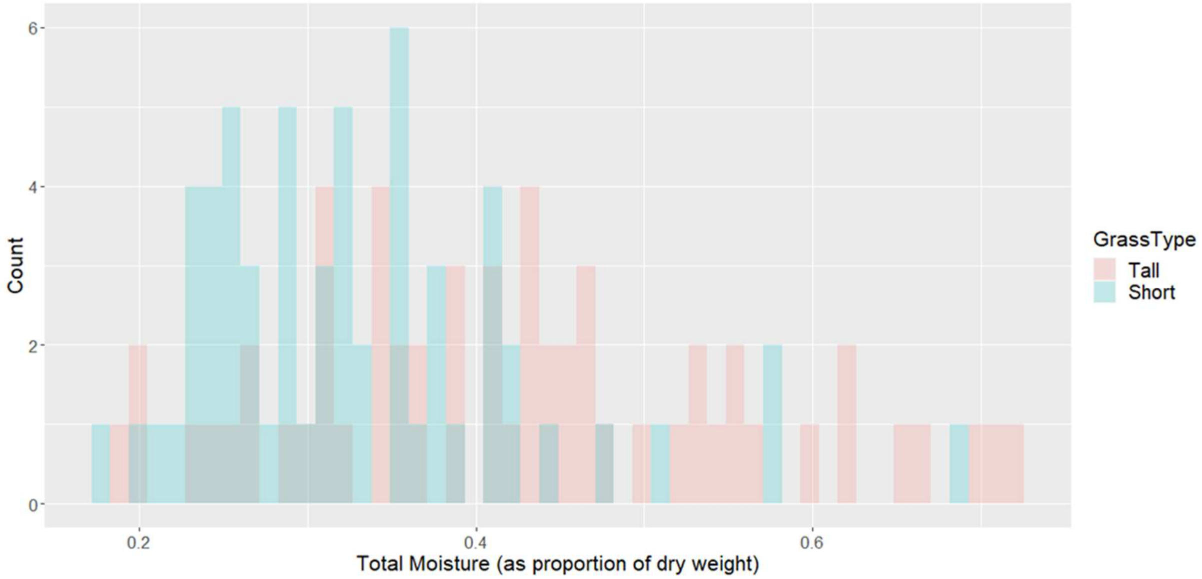

Figure 3.1. Moisture Distribution by Grass Type

It is not obvious whether the reflectance in the tall grass will respond to the moisture of the entire height of the vegetation or only the moisture in the upper portion since the images are taken from above. To determine which moisture metric seemed most representative, we compared the correlation of each with NDVI, the most commonly-used vegetation health metric.

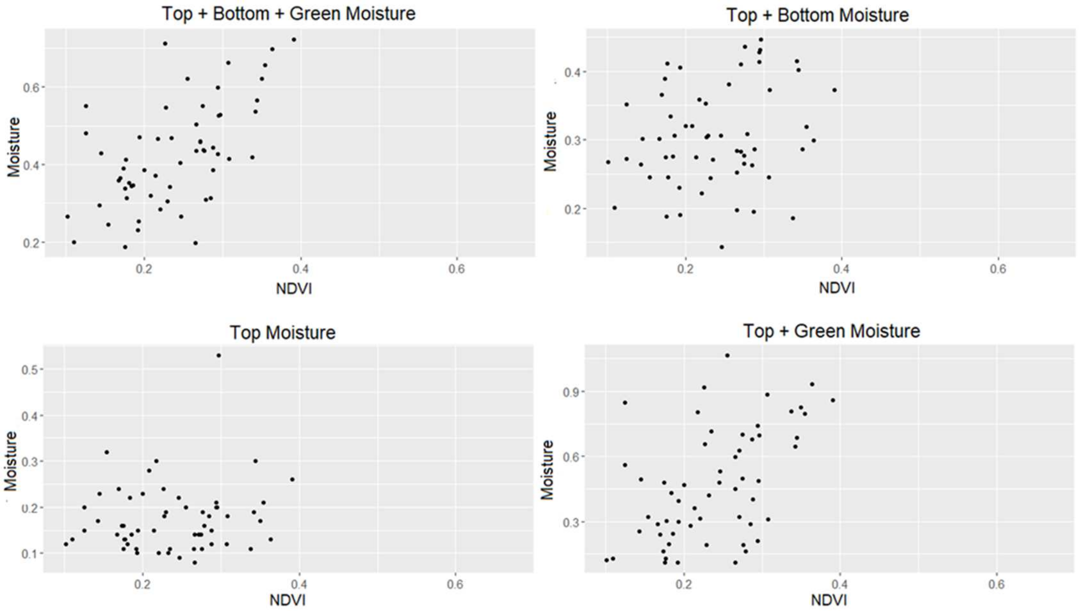
Top + Bottom + Green Moisture

Top + Bottom Moisture

Top Moisture

Top + Green Moisture

Figure 3.2. Comparison of Moisture Metrics for Tall Grass

Figure 3. shows that for the tall grass, taking into account all of the vegetation in the plot gives the clearest relationship with NDVI. It is also clear from this plot that the greener vegetation has a strong influence on the NDVI. For the shorter grass (Fig. 3.3), the relationship is weaker overall, but it is still improved by including the green moisture. For subsequent analysis, the total moisture of the plots was used.

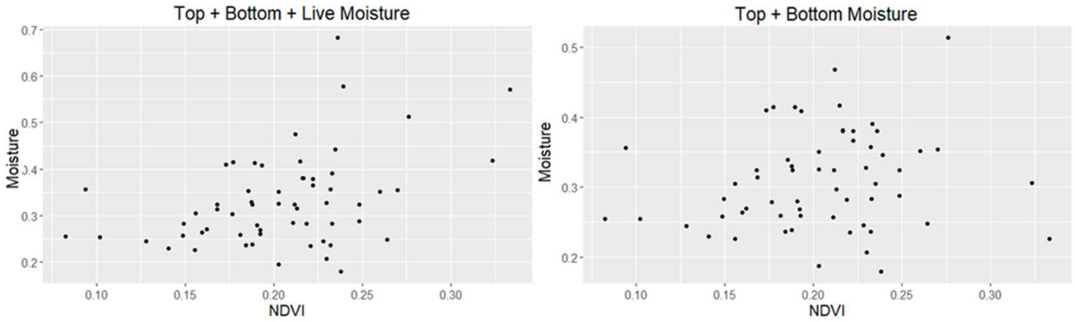
Top + Bottom + Live Moisture

Top + Bottom Moisture

Figure 3.3. Comparison of Moisture Metrics for Short Grass

3.2 MODEL BUILDING

Table 3.2 shows the results of PCA using the mean reflectance for every band except the SWIR band, since the SWIR data was much less correlated with the other wavelengths than they were with each other (.2-.4 as opposed to .6-.9 between the others).

Table 3.2. Results of PCA

Band	**PC1**	**PC2**	**PC3**	**PC4**
Blue	.408	.746	-.474	-.225
Green	.460		.622	-.625
Red	.462	.222	.403	.670
Red Edge	.438	-.317	-.185	.296
NIR	.464	-.540	-.438	-.152
% Variation	**.848**	**.090**	**.034**	**.018**

The first four principal components are included because together they account for 99% of the variation in the reflectance data.

Table 3.2. Summary of Models Based on Vegetation Indices and PCs

Index	**r^2**	**Slope**	**Intercept**	**p-value**
NDVI	.329	1.189	0.115	0.000
NDWI	.014	-0.085	0.374	0.119
VARI	.174	0.571	0.377	0.000
NDGR	.174	0.956	0.376	0.000
NDVI + Weight	.431	0.930 0.001	0.093	0.000
NDWI + Weight	.307	-0.027 0.002	0.253	0.000
VARI + Weight	.303	0.340 0.001	0.285	0.000
NDGR + Weight	.304	0.570 0.001	0.285	0.000
PC2	.336	-0.124	0.380	0.000
PC2 + PC4	.387	-0.133 -0.106	0.381	0.000
PC2 + PC4 + Weight	.452	-0.105 -0.091 0.001	0.315	0.000

Table 3. summarizes the results of the regression of four different vegetation indices and principal components on field moisture measurements. The NDWI terms are not significant, but every other term is ($p<.05$). NDVI, VARI, and NDGR are all significantly positively correlated with moisture, but NDWI is not. All of the models are improved by including the total weight of the field sample, a metric used to account for increased moisture in denser vegetation, which will be justified below. NDVI accounts for far more (32.9%) of the variation in fuel moisture than the other two significant indices based on visible wavelengths alone (VARI and NDGR both explain 17.4%).

As expected, PC1 was not a significant predictor of moisture in a model that included both principal components and weight, and PC3 also was not a significant predictor in a model including all four components. PC2 + PC4 along with weight performed similarly to but slightly better than the model with NDVI and weight.

Table 3.3. Summary of Models for Separate Vegetation Types

Index	**Dominant Species**	**r^2**	**Slope**	**Intercept**	**p-value**
NDVI	*A. elatius*	.340	1.157	0.150	0.000
	A. stolonifera	.154	0.843	0.159	0.001
VARI	*A. elatius*	.037	0.403	0.406	0.078
	A.stolonifera	.128	0.438	0.351	0.002
NDVI + Weight	*A. elatius*	.372	1.045 0.001	0.081	0.000
	A. stolonifera	.258	0.717 0.001	0.121	0.000
PC2 + PC4 + Weight	*A. elatius*	.435	-0.141 -0.080 0.001	0.288	0.000
	A. stolonifera	.316	-0.084 -0.079 0.001	0.295	0.000

Additionally, separate models were developed for the two grass types to determine if modeling each separately was more effective. A summary of a few of these is shown in Table 3.3. None of the models for individual grass types was an improvement over the pooled model for PC2, PC4, and total weight. The principal components also performed similarly to NDVI for the models that treated the grass types separately. The best model was therefore the pooled model that included PC2, PC4, and vegetation weight ($r^2 = .45$). Its AIC was also slightly lower than the NDVI model (-219 as opposed to -216). Figure X shows this model fit, which is similarly good for both vegetation types. The equation of this model is as follows:

$$LMFC = -0.061\,R - 0.058\,B + 0.057\,G + 0.060\,RE + 0.071\,NIR + 0.001\,Weight + .315 \quad (3.1)$$

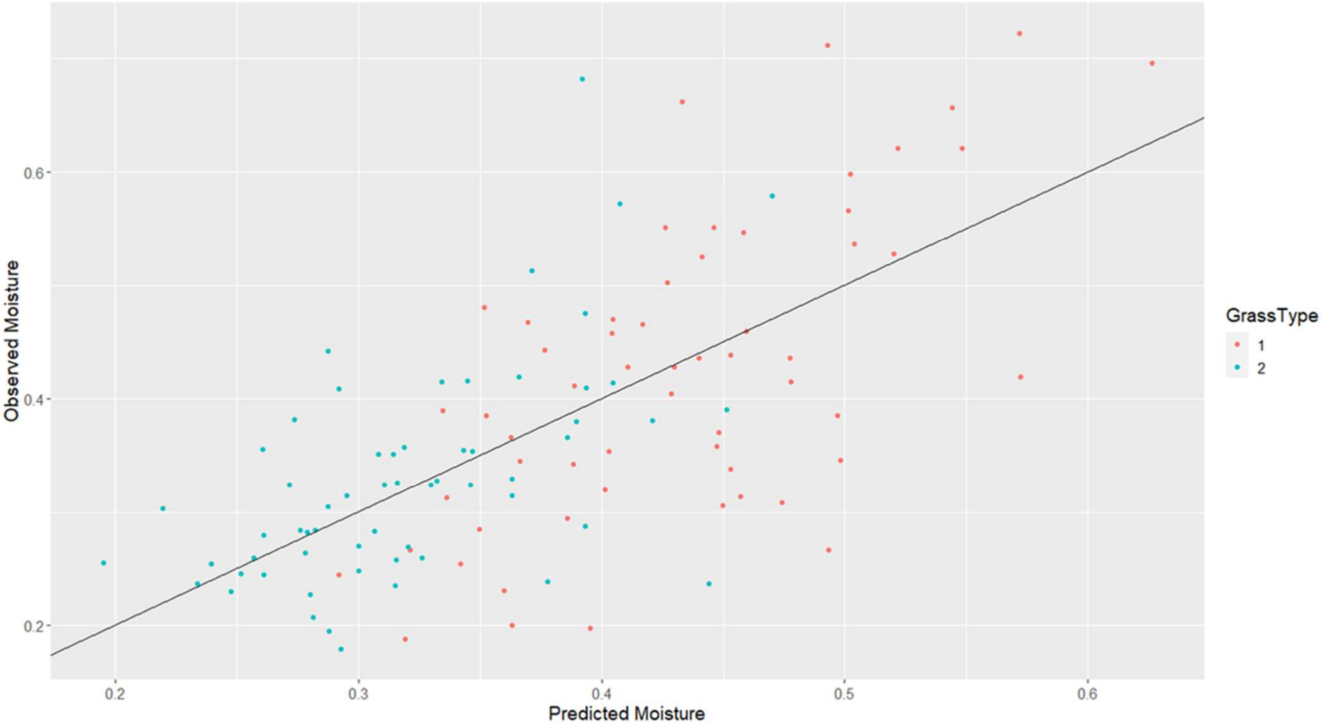

Figure 3.4. Model Fit by Grass Type

Chapter 4. DISCUSSION

4.1 COMPARISON OF MODELS

In contrast to previous studies using MODIS data and shrublands/chapparal, this study does not show much predictive power for VARI and NDGR [24,29,54]. While some research shows that VARI is a better predictor than NDVI in these other ecosystems [31], the present study is in agreement with many existing studies in grasslands. Others have also found that NDVI outperformed VARI in grasses, with mixed results for NDWI predictions [26,29,55]. This model has similar performance to the results of an existing study by Lim, et al. utilizing NDVI from UAV-mounted sensors to predict moisture over a similar range of values in cut hay [56]. This study extends the relevance of this method, as much of the existing research does not focus on using UAVs to obtain data about fire fuels and instead utilizes satellite imagery and/or focuses on agricultural products rather than mixed vegetation.

This study also shows improved model performance by using PCA, a less common way of representing reflectance data than the more traditional vegetation indices. Based on the loadings, it appears that PC1 represents the overall brightness of the plots, a largely geometric factor that would ideally be excluded from the model. These results show that PCA has potential to separate the effects of geometry and overall brightness from vegetation characteristics that are more closely related to fuel moisture. PC2 is dominated by a positive relationship between moisture and near infrared/ red edge and a negative relationship with blue (based on the negative model coefficient), and PC4 represents a negative relationship with red and a positive relationship with green. PC2 could represent lower moisture content, since the region of .7-.8 μm is a diagnostic band for leaf moisture. In addition, the red edge band may be of particular importance in this study as changes in reflectance in this band are particularly associated with senescence [57]. Therefore, it is interesting and perhaps expected that it also factors into the model. It is unusual, however, that the blue wavelength is such a large part of this principal component when it tends to have only small amounts of correlation with moisture [24]. In this particular ecosystem, however, the scotch broom and some of the other greener vegetation had much lower blue reflectance than the drier grass species. PC4 provides information that intuitively would be related to fuel moisture and is similar to NDGR—grass which is more green and less red is generally moister. Future work is necessary to determine whether PCA results outperform NDVI in different datasets, though it offers the advantage of easily including all available wavelengths (including red edge, which is not a term in many typical indices) in a flexible way that could easily make use of different model parameters for different ecosystems.

The performance of the models discussed in this study is clearly better for the tall grass. In the study area with shorter vegetation, there was more exposed soil. It is likely that soil reflectance is interfering with creating an accurate model in this area and that accuracy could be further improved by accounting for the effects of soil in plots that have less complete vegetation cover. Soil reflectance has been addressed in the past with MSAVI, an index which attempts to correct for varying amounts of vegetation cover [58].

4.2 IMPLICATIONS FOR SENSOR SELECTION

Based on the results of this study, utilizing near-infrared sensors is useful for predicting vegetation moisture compared with using visible wavelengths alone. On the other hand, it does not provide evidence that utilizing this SWIR sensor improves the results. It is possible that another sensor with a slightly different range would perform better. The upper end of the range of the Tau is 1.3 µm, whereas a characteristic reflectance band of water is closer to 1.4 µm [57]. Some studies utilizing MODIS bands use band 5, which is 1.23-1.25 µm, to calculate NDWI and obtain modest results, though NDVI and VARI were still both better predictors in almost all cases [23,24]. The original formulation of NDWI defines it using the same wavelength as MODIS band 5 [45]. Though the range in this study includes this wavelength, it is much larger, with a band width of 600nm. It is likely that other effects occur at the lower end of the sensor range which obscure the intended impacts of water absorption. A sensor with a narrower band would likely improve the ability to directly measure water thickness. This is simple when one is making use of satellite data, for which this narrow band is available, but less straightforward when purchasing a small UAV-mounted sensor. However, there are many readily available NIR sensors, including the one used in this study, which are relatively inexpensive and user-friendly. The ability to estimate moisture using visible/NIR sensors alone is a significant management opportunity.

4.3 FUTURE IMPROVEMENTS OF METHOD

The results of this analysis are promising in terms of obtaining spatially explicit fuel moisture data for fire modeling. Due to logistical constraints, this study utilized vegetation with a range of moisture that was significantly smaller than other studies. Previous studies predicting moisture in grasses developed models with r^2 values of .7-.9, but contained 200%-300% moisture ranges, as opposed to the less than 80% moisture range in this study [26,29]. Even some models built on vegetation that experiences less change in moisture content than grass, such as shrubs or chapparal, spanned at least a 100% range of vegetation moisture [23,24]. For this reason, it is not surprising that the best model explained only a modest proportion of the vegetation moisture. Examining the effect of the "green" moisture makes it clear that the few very green plants had a large effect on the analysis. In some ways, this is a limitation of using UAV data, as opposed to satellite data which can be used to obtain separate measurements throughout an entire season or more without much additional data collection effort. However, in future work, this problem could be addressed by taking measurements throughout the fire season to develop the model. In fact, early-season data can be particularly relevant for prescribed burning. Given these limitations, this study confirms existing research utilizing remote sensing data to estimate moisture while extending it to a different application.

In this study, the weight of the vegetation proved to be a useful predictor of vegetation moisture. Previous work shows that biomass data can be obtained using photogrammetric methods and UAV-mounted sensors, making this a promising avenue of inquiry even without field measurements of biomass [59]. In a 2018 study by Viljanen et al, modest to good biomass estimates were obtained for barley using only photogrammetric information and visible reflectance data [60]. In another study, strong correlations were found between photogrammetry data and wheat biomass [61]. Since these measurements can be obtained using the same sensors as the moisture measurements and these geometric properties of the vegetation would also be necessary for other aspects of fire modeling, it is a promising avenue for further investigation.

4.4 FUTURE WORK

The rasters generated by this methodology have more than sufficient resolution for use as an input to a model such as FDS. To make this process operationally viable, there are many avenues for future work.

The data collection methods detailed in this paper could be improved using the methods described above. It is also possible that the development of UAV-compatible SWIR sensors will allow for more accurate moisture predictions. In some cases accounting for soil moisture may improve the results.

In addition, work to determine the sensitivity of fire models to the resolution and range of moisture in the input rasters would be valuable. More investigation into different ecosystems and the spatial variability of moisture, as well as its effect on fire behavior, will be necessary to develop a more broadly applicable model. It would be useful to determine for which vegetation types and in which situations moisture resolution is more influential to fire behavior in order to prioritize data-collection and model development.

Photogrammetric estimates of biomass could be used in conjunction with a method such as the one described in this paper to create a workflow for generating fuel data model inputs. This could allow some work toward model validation, by recording remote sensing data at a site as well as fire behavior data during a pre-scribed burn and comparing the fire behavior to the results of a simulation using these model inputs.

4.5 CONCLUSIONS

This method has promise both as a way of validating fire models and of obtaining moisture estimates for predictive modeling in the future. Flying a UAV over an area of interest can eliminate logistical constraints when compared to either relying on satellite imagery or utilizing traditional field sampling methods. For example, collecting the fuel moisture for one of the 120 1 x 2 m^2 sample plots in this study took approximately twice as long as a UAV flight over the entire study area. While it would be challenging to collect accurate moisture data immediately before a fire using traditional moisture sampling methods, using UAV-based data-collection methods could enable obtaining accurate moisture data much closer to a prescribed burn or other period of interest.

APPENDIX A: ADDITIONAL ANALYSIS

I repeated the principal component analysis with the SWIR values, which was only made possible by eliminating any plots for which the SWIR values did not exist. This resulted in 107 instead of 120 samples. This helped address the question of whether it is useful to include the more expensive SWIR camera in similar future studies.

Table A.3. PCA Loadings Including SWIR

	R	G	B	RE	NIR	SWIR	Prop. Variance	Cumulative Var.
Comp. 1	.451	.448	.395	.456	.434	.210	.736	.736
Comp. 2	.156	.138	.280			-.933	.148	.884
Comp. 3	.185	-.121	.708	-.305	-.528	.279	.068	.952
Comp. 4	.392	.625	-.450	-.215	-.450		.027	.979

In this case, much more of the variance was explained by the second component, which was heavily influenced by the SWIR wavelength. It seems to be very disparate from the other wavelengths, which is reflected in the fact that it is much less correlated with the other wavelengths than they are with each other. It is a little less obvious in this case what the physical implications of the PCA components are-- the first one is no longer quite as good of an approximation of overall brightness, and the second and third both might have some aspects of plant stress mixed up in them.

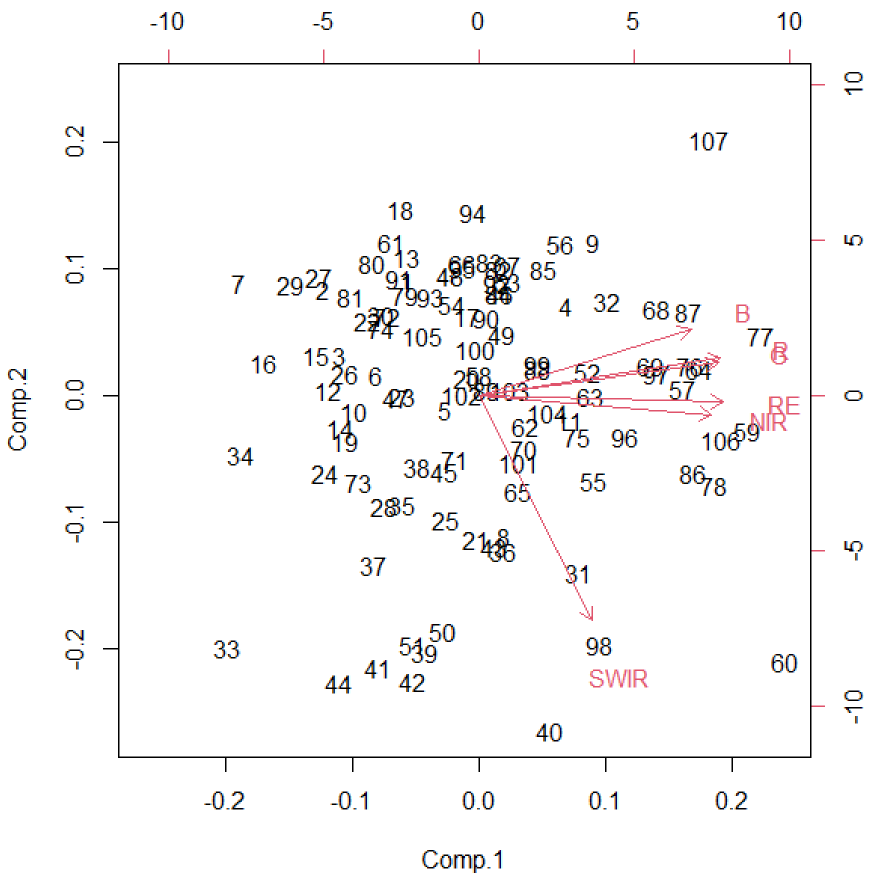

Figure A.1. PCA Components with SWIR

The above plot shows the first and second principal components from this analysis, where the second component is dominated by the SWIR wavelength.

To explore other methods of predicting grass moisture using the principal components just developed, I built a regression tree using the first four principal components as well as the total weight of the grass, which I also expected to have some effect since more dense grass retains more moisture.

I built a classification tree using the total moisture, calculated as above. I used 100 multiple cross-validations and picked the resulting tree by hand from the relative error plot based on the lowest error (which in both of the following trees was far lower than the error for other candidates).

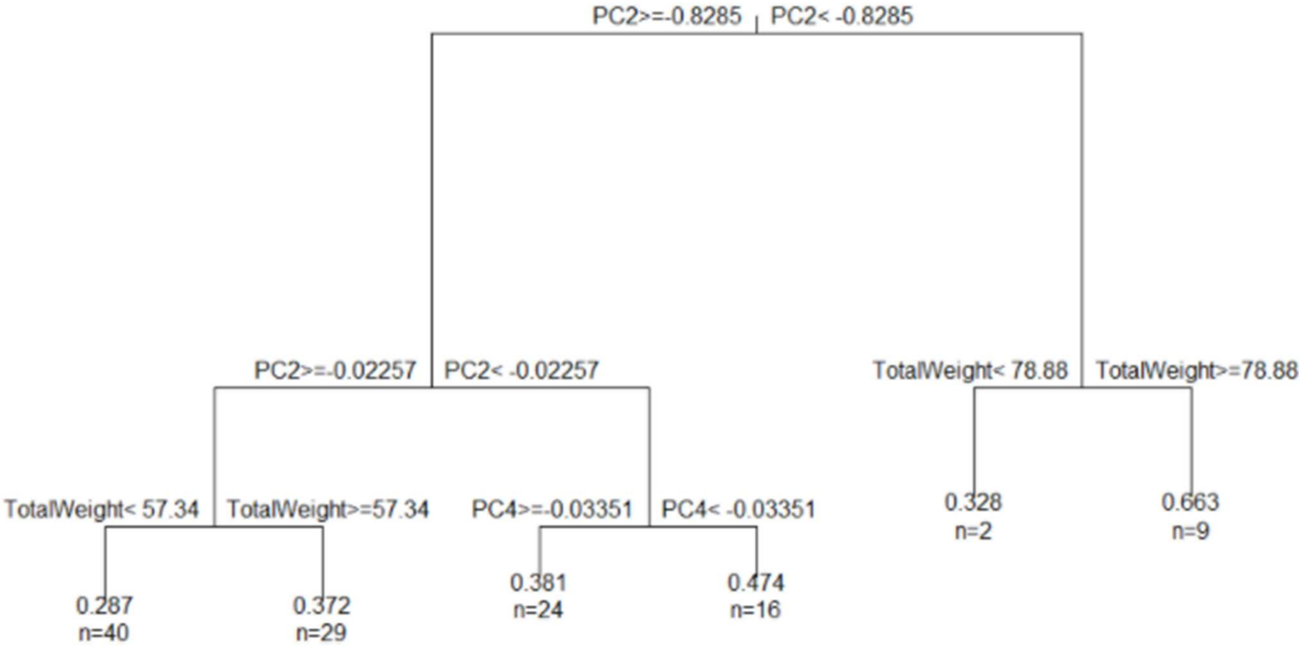

Figure A.2. Regression Tree Based on Principal Components

The resulting tree is mostly driven by the second principal component. It also relies somewhat on the total weight. As expected, PC1 does not play a role in the regression. However, the error is quite high, .408 with a cross-validated error of .821, which is very high relative to the moisture values I am trying to predict. I also tried making a regression tree using a separate term for the SWIR values.

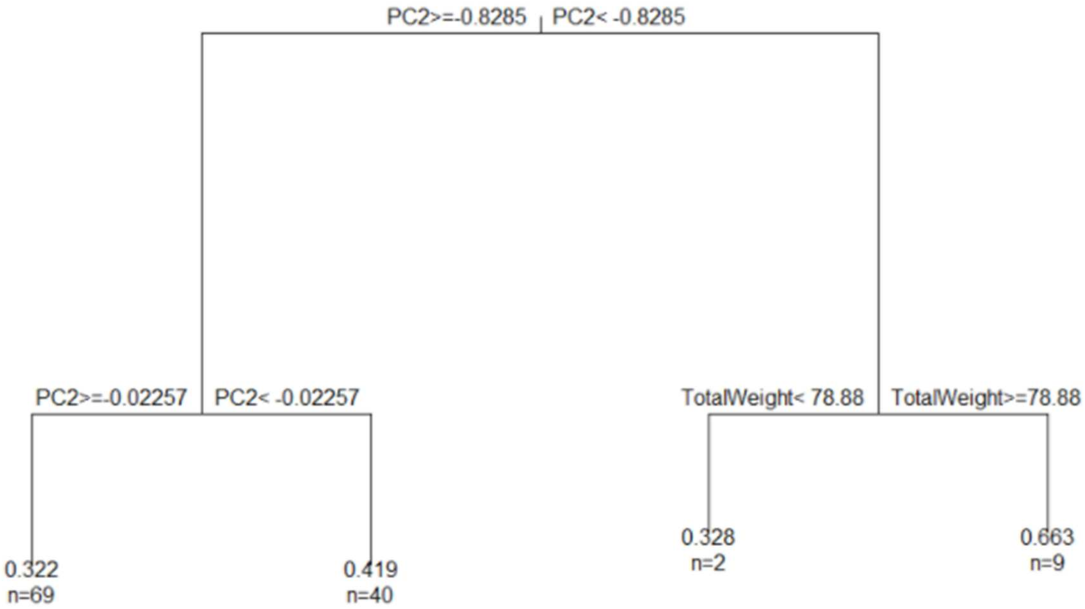

Figure A.2. Regression Tree Based on Principal Components Including SWIR

This one has even higher error (.51, cross validated=.86), and does not even make use of the SWIR data, so it is evident that including the SWIR data does not improve the results of the analysis in this case.

APPENDIX B: FIELD WORK METHODOLOGY

0. Equipment Checklist

1. Micasense camera and peripherals
2. Tau camera, its associated USB and video cables
3. USB video converter
4. BNC female to RNC male converter
5. At least 3 USB battery packs
6. 2 USB-C cables and extras
7. Raspberry pi
8. Calibration panel for Micasense
9. USB Monitor
10. USB mouse/keyboard
11. Computer for running flight software
12. Computer for checking cameras/data
13. Inverter/car that can be used with inverter
14. Drone and associated items
15. Two each of SD cards formatted for the raspberry pi and the Micasense, kept separately
16. SD card USB adapter
17. Tape measure
18. Several shears
19. Airtight ziploc bags
20. Several coolers
21. Aerial markers/GCPs

22. Alignment objects
23. PVC pipe and fittings for plot establishment
24. 1’ PVC pipe segments for field sample stratification
25. Gloves
26. Sharpies
27. Duct tape
28. Lens cleaner
29. USB router in case it is needed for the flight control laptop
30. Survey-grade GPS

1. Site Establishment

The study area consisted of 60 plots on each side of a road, in 6 rows/side of ten plots each. The rows were spaced 2 meters apart, and then a tape measure was used to place a plot every two meters. When bare ground or very poor drainage (such as a ditch) was encountered, this plot location was skipped. The plots were delineated by 1m square PVC frames with posts sticking out of the west corner. When establishing the plots, the frame was constructed within the grass to avoid crushing the grass. In plot establishment and in collecting field data, stepping inside the plot was avoided. Each plot was labeled with a number according to a consistent numbering scheme (plots 1-60 were “tall grass” and plots 61-120) were “short grass.”

The workspace for setting up the drone, with a table, laptops, etc was established at the north end of the test site. The calibration panel for the micasense was set up near this site. Some good things to have on hand for emergencies include extra USB battery packs, an extra laptop, and an inverter.

The overall location of the test site was delineated with wooden aerial placards marked with the cardinal direction. Objects to aid in image alignment were scattered around the area (pool noodles and bi-colored metal objects). Sixteen ground control points made of steel sheets with black "x's" drawn on them were also scattered throughout the study area. Throughout the rest of this process, the locations for these GCPs were recorded using the GPS unit.

The steps below were conducted once in the morning flight and once in the afternoon.

2. Camera testing/setup

The following checklist was performed before each flight:

a. Check the micasense and ensure that it has an empty, properly formatted SD card.
   1. An SD card with a write speed of at least 100MB/s should be used, ideally 32+GB, or images will be skipped in recording.
   2. The status of the SD card can be viewed in the Micasense web app, which is accessible by connecting to the camera's wifi network and navigating to the IP address listed on the camera.

b. Check/set the Tau
   1. Using the windows software that comes with the camera (link below) and a windows computer, establish the correct exposure settings for the field. In this study, the minimum amount of contrast was used. The settings can be tested using any camera app on the computer.

https://www.dropbox.com/s/mu6yfcomvcbbtdy/CameraControllerSetup.msi?dl=0

   2. The lens of the Tau should be cleaned with lens wipes.
   3. The focus should be set to infinity.

c. Attach both the Tau and the Micasense to the drone

d. Drone setup up to this point is as per AFSL procedures

e. The micasense is connected to its own power source, and the Tau is connected via 2 USB ports to the raspberry pi, which also has a separate power source. All of these things must be attached to the drone, an area that could be improved in the future. A simple diagram of the electronics is below.

3. Start Recording

A wireless USB keyboard and a USB monitor were used to start the Tau using ffmpeg from the raspberry pi terminal, using the command below:

```
ffmpeg -f v4l2 -r 25 -s 640x480 -i /dev/video0 out.avi
```

The Micasense was initiated from the web app. The capture rate should be set to once per second (the fastest it goes).

4. Flight

This study used an M600 drone and UGCS flight control software. The drone setup and flight safety procedures are standard AFSL procedures. The flight control settings were as follows for both flights. At the start of the flight, the drone was flown over the calibrated reflectance panel.

a. Flight pattern: double-grid

b. Side-lap: 80%

c. Overlap: 85%

d. Height: 52 ft.

e. Speed: 3 m/s

Note: the overlap was calculated automatically by the software for the Micasense and did not reflect sufficient side-lap for the Tau. This issue should be resolved in future work.

5. Data Quality Check

a. When the drone landed, it was brought over to the table so that the raspberry pi could be reconnected to the monitor and keyboard to end the video recording. The video was then viewed on the USB monitor to ensure successful recording and data quality.

b. Then, the drone and peripherals were unplugged/powered off.

c. The SD card was removed from the Micasense and plugged into a laptop for a quality check and to remove the images and put them on the computer in an appropriate folder.

6. Field Sample Collection

a. As quickly as possible after the flight, the field samples were recorded. This was accomplished by randomly generating the list of plots to be collected after each flight and then assigning a subset of these plots to each person. The bags were also partially prelabeled for efficiency.

b. Each plot was destructively sampled and placed into three bags:

Live: Scotch Broom, ferns and very green grass were collected separately and placed in this bag. (These were not very abundant.)

Top: Using a 1 foot long PVC pipe placed vertically, every remaining piece of vegetation above this height was placed into this bag.

Bottom: The rest of the vegetation was collected in this bag, except mosses, roots, and grass very covered in soil.

c. Each bag was carefully sealed, labeled with the plot, grass type, initials of the collector, sample type, and time and date collected, and placed in a cooler.

d. If a piece of vegetation was only partially included in the plot, the collector included whatever parts of the plant were “visually” in the plot. For example, if grass had roots outside the plot but the upper portion fell within, it would be cut off at the point it entered the plot and bagged.

7. Field Sample Processing

The field samples were taken back to the USFS lab in Seattle, where they were weighed, oven-dried, and weighed again to calculate fuel moisture.

APPENDIX C: PROCESSING PROCEDURE

1. Extracted Tau images from video using ffmpeg on the raspberry pi, at 8fps and using an uncompressed format (like .bmp)

Note for future work: There are still compression artifacts in the images, this is because a lossless video codec should have been used instead of the default, this would be changed in the ffmpeg settings when initially recording.

2. Removed images from both Micasense and Tau data from before and after flight, as well as any obvious exposure issues (extremely occasional very overexposed or totally black images)
3. Stitched together micasense images in Agisoft using default settings (make sure to import it as a multi-camera system)
    1. Aligned photos with high accuracy, generic preselection, and reference preselection, key point limit of 80,000 and tie point limit of 4,000.
    2. Created a high-quality mesh with medium face count and constructed orthomosaics with the mesh as the surface and mosaic blending mode.
4. Calibrated reflectance in the Micasense images
    1. First, the reflectance panel was located in an image and put in a separate folder called “Calibration images”
    2. Then, applied a mask and removed the rest of the image except the panel
    3. The calibration values, obtained from the manufacturer, are below:

    For RedEdge-MX with serial RX01 or lower, all RedEdge-M and RedEdge 3 cameras, and Altum cameras with serial AL04 or lower:

blue	*0.97*	*97.32%*
green	*0.98*	*97.76%*
red	*0.98*	*98.37%*
re	*0.99*	*98.54%*
nir	*0.99*	*98.56%*

5. Set the raster transform to each band individually, set them to the same scale and a black and white gradient, and then exported them as individual band rasters. (Also created a visible light ortho because it's easier to look at)
6. Stitched together Tau images
    1. Similar to micasense, but it only partially aligned, so kept moving the unaligned images into a new chunk, realigning, moving the yet remaining images into another chunk, etc, until there were ~15-20 chunks of partially mosaiced images
    2. Aligned photos with high accuracy, generic preselection, and reference preselection, key point limit of 80,000 and tie point blank (no limit).
    3. Created a high-quality mesh with medium face count and constructed orthomosaics with the mesh as the surface and mosaic blending mode.
    4. Exported orthomosaics, numbering them using the numbers of the photos from which they originated (there's only one band)
7. Aligned everything in ArcPro
8. Used GCP coordinates to georeference the visible light orthomosaic, and field notes to identify the correct GCPs

9. Imported the other Micasense orthos and align them using georeferencing (affine transform) with 9 points
10. Aligned the partial Tau images (affine transform) using markers and clues from photo numbers, didn't use them if the alignment was too poor or uncertain (scrapped if <4 points to align them or if the imagery was obviously distorted)
11. Mosaiced the Tau images into one big raster using the minimum value so the high values are not included when the white border of a raster overlaps with another.
12. Created polygons for the plot locations
    1. Drew them by hand, as close to right inside the PVC as possible, didn't force them to be squares since occasionally there was a little warping in the image/the plot was slightly askew
    2. Added a value for plot number to the attribute table and numbered the plots based on field notes
13. Remove values in plots above a certain threshold using "set null" function
    1. These represent the very reflective PVC pipes included due to small misalignments
    2. This process used each layer separately as both the "conditional" and "false" raster, with an equation to set values to null greater than a certain threshold.
    3. The threshold values were different depending on the wavelength, and they were obtained by exploring the image to find what value would reliably exclude PVC pipes but not bright grass (at this stage the values are still scaled 0-255 representing 0-100% reflectance).
        1. Removed >225 for SWIR

    2. Removed >180 for NIR and rededge
    3. Removed >140 for the visible wavelengths
14. Used zonal statistics to create a table with mean and standard deviation for each plot in each wavelength for each time of day.
15. The attribute tables from the zonal statistics were all joined to the plot polygons on Plot ID
16. Export table was used to create a csv file of these values
17. Further texture analysis in MATLAB (see code)
18. Statistical analysis in R, along with field data table (see code)

APPENDIX D: R CODE

MAKE_DF.R

```
make_df<-function(imagery_data,field_data,texture_data){
  ##need to make a df with the top, bottom, and live moisture and weight for each
  ##plot as well as the relevant imagery information, calculate time since flight,
  ##also location

  #sample period 1 is AM, 2 is PM
  #sample type 1 is top, 2 is bottom, 3 is live
  #1-60 are tall and 61-120 are short

  library(vegan)

  df <- data.frame(Index=integer(),
                MoistureTop=double(),
                WeightTop=double(),
                WeightBottom=double(),
                MoistureBottom=double(),
                MoistureLive=double(),
                TimeSinceFlightTop=integer(),
                TimeSinceFlightBottom=integer(),
                GrassType=integer(),
                SamplePeriod=integer(),
                R=double(),
                G=double(),
                B=double(),
                RE=double(),
                NIR=double(),
                SWIR=double(),
                R_r=double(),
```

```
        G_r=double(),
        B_r=double(),
        RE_r=double(),
        NIR_r=double(),
        SWIR_r=double(),
        X=integer(),
        Y=integer(),
        TopTransformed=double(),
        WeightLive=double(),
        Texture=double(),
        Texture_r=double()
)

##turn field moisture into series of things with one entry/plot
##rewrite this to not use for loops, it's ugly
top_moisture=c()
bottom_moisture=c()
live_moisture=c()
sample_period=c()
X=c()
Y=c()
top_time_collected=c()
bottom_time_collected=c()
top_weight=replicate(120,0)
bottom_weight=replicate(120,0)
live_weight=replicate(120,0)
range=c(1:294)
for (n in range){
  if (field_data$Sample.Type[n]==2){
    bottom_moisture[as.numeric(field_data[n,1])]=field_data$Fuel.Moisture[n]
```

```
      bottom_weight[as.numeric(field_data[n,1])]=field_data$Dry.Gross.Weight[n]-
field_data$Dry.Container.Weight[n]
      sample_period[as.numeric(field_data[n,1])]=field_data$Sample.Period[n]
      X[as.numeric(field_data[n,1])]=field_data$X[n]
      Y[as.numeric(field_data[n,1])]=field_data$Y[n]
      bottom_time_collected[as.numeric(field_data[n,1])]=field_data$Time.Collected[n]
    }
    if (field_data$Sample.Type[n]==1){
      top_moisture[as.numeric(field_data[n,1])]=field_data$Fuel.Moisture[n]
      top_weight[as.numeric(field_data[n,1])]=field_data$Dry.Gross.Weight[n]-
field_data$Dry.Container.Weight[n]
      top_time_collected[as.numeric(field_data[n,1])]=field_data$Time.Collected[n]
    }
    if (field_data$Sample.Type[n]==3){
      live_moisture[as.numeric(field_data[n,1])]=field_data$Fuel.Moisture[n]
      live_weight[as.numeric(field_data[n,1])]=field_data$Dry.Gross.Weight[n]-
field_data$Dry.Container.Weight[n]
    }
  }
```

```
  ##put field moisture and corresponding imagery data in dataframe
  ##time for AM flight was 939
  ##time for PM flight was 1506
  for (n in 1:120){
    df[n,"Index"]=n
    df[n,"MoistureTop"]=top_moisture[n]
    df[n,"MoistureBottom"]=bottom_moisture[n]
```

```
df[n,"MoistureLive"]=live_moisture[n]
df[n,"WeightTop"]=top_weight[n]
df[n,"WeightBottom"]=bottom_weight[n]
df[n,"WeightLive"]=live_weight[n]
df[n,"X"]=X[n]
df[n,"Y"]=Y[n]
df[n,"SamplePeriod"]=sample_period[n]
if (sample_period[n]==1){
  df[n,"TimeSinceFlightTop"]=top_time_collected[n]-939
  df[n,"TimeSinceFlightBottom"]=bottom_time_collected[n]-939
  df[n,"R"]=imagery_data[n,"AM_R_M"]
  df[n,"G"]=imagery_data[n,"AM_G_M"]
  df[n,"B"]=imagery_data[n,"AM_B_M"]
  df[n,"RE"]=imagery_data[n,"AM_RE_M"]
  df[n,"NIR"]=imagery_data[n,"AM_NIR_M"]
  df[n,"SWIR"]=imagery_data[n,"AM_SWIR_M"]
  df[n,"R_SD"]=imagery_data[n,"AM_R_SD"]
  df[n,"G_SD"]=imagery_data[n,"AM_G_SD"]
  df[n,"B_SD"]=imagery_data[n,"AM_B_SD"]
  df[n,"RE_SD"]=imagery_data[n,"AM_RE_SD"]
  df[n,"NIR_SD"]=imagery_data[n,"AM_NIR_SD"]
  df[n,"SWIR_SD"]=imagery_data[n,"AM_SWIR_SD"]
  df[n,"Texture"]=texture_data[n,"texture_AM"]


}
if (sample_period[n]==2){
  df[n,"TimeSinceFlightTop"]=top_time_collected[n]-1506
  df[n,"TimeSinceFlightBottom"]=bottom_time_collected[n]-1506
  df[n,"R"]=imagery_data[n,"PM_R_M"]
  df[n,"G"]=imagery_data[n,"PM_G_M"]
```

```
      df[n,"B"]=imagery_data[n,"PM_B_M"]
      df[n,"RE"]=imagery_data[n,"PM_RE_M"]
      df[n,"NIR"]=imagery_data[n,"PM_NIR_M"]
      df[n,"SWIR"]=imagery_data[n,"PM_SWIR_M"]
      df[n,"R_SD"]=imagery_data[n,"PM_R_SD"]
      df[n,"G_SD"]=imagery_data[n,"PM_G_SD"]
      df[n,"B_SD"]=imagery_data[n,"PM_B_SD"]
      df[n,"RE_SD"]=imagery_data[n,"PM_RE_SD"]
      df[n,"NIR_SD"]=imagery_data[n,"PM_NIR_SD"]
      df[n,"SWIR_SD"]=imagery_data[n,"PM_SWIR_SD"]
      df[n,"Texture"]=texture_data[n,"texture_PM"]

    }
    if (n<61){
      df[n,"GrassType"]=1 #tall
    }
    if (n>60){
      df[n,"GrassType"]=2 #short
    }
  }

  ##need to scale for PCA
  df[17:22] <-scale(df[,11:16])
  df[28] <-scale(df[,27])
  ##df[,17:22]<-decostand(x=df[,16:21], method="total", MARGIN=2, na.rm = FALSE)
  ##df[,26:31]<-decostand(x=df[,17:22], method="total", MARGIN=2, na.rm = TRUE)

  return(df)
}
```

IMPORT_MOIST.R

```
import_moist<-function(imagery_data_path){
  imagery_data=read.csv(imagery_data_path)
  imagery_data["PM_RE_M"]=imagery_data["PM_RE_M"]/255
  imagery_data["PM_RE_SD"]=imagery_data["PM_RE_SD"]/255
  imagery_data["PM_NIR_M"]=imagery_data["PM_NIR_M"]/255
  imagery_data["PM_NIR_SD"]=imagery_data["PM_NIR_SD"]/255
  imagery_data["PM_R_M"]=imagery_data["PM_R_M"]/255
  imagery_data["PM_R_SD"]=imagery_data["PM_R_SD"]/255
  imagery_data["PM_G_M"]=imagery_data["PM_G_M"]/255
  imagery_data["PM_G_SD"]=imagery_data["PM_G_SD"]/255
  imagery_data["PM_B_M"]=imagery_data["PM_B_M"]/255
  imagery_data["PM_B_SD"]=imagery_data["PM_B_SD"]/255
  imagery_data["PM_SWIR_M"]=imagery_data["PM_SWIR_M"]/255
  imagery_data["PM_SWIR_SD"]=imagery_data["PM_SWIR_SD"]/255
  imagery_data["AM_RE_M"]=imagery_data["AM_RE_M"]/255
  imagery_data["AM_RE_SD"]=imagery_data["AM_RE_SD"]/255
  imagery_data["AM_NIR_M"]=imagery_data["AM_NIR_M"]/255
  imagery_data["AM_NIR_SD"]=imagery_data["AM_NIR_SD"]/255
  imagery_data["AM_R_M"]=imagery_data["AM_R_M"]/255
  imagery_data["AM_R_SD"]=imagery_data["AM_R_SD"]/255
  imagery_data["AM_G_M"]=imagery_data["AM_G_M"]/255
  imagery_data["AM_G_SD"]=imagery_data["AM_G_SD"]/255
  imagery_data["AM_B_M"]=imagery_data["AM_B_M"]/255
  imagery_data["AM_B_SD"]=imagery_data["AM_B_SD"]/255
  imagery_data["AM_SWIR_M"]=imagery_data["AM_SWIR_M"]/255
  imagery_data["AM_SWIR_SD"]=imagery_data["AM_SWIR_SD"]/255
  return(imagery_data)
}
```

MODEL_BUILDING.R

```
library(dplyr)
library(ggplot2)
library(gridExtra)
##import
##note: plot 54 collected incorrectly
##plot 115 is total moisture and not separate, should not affect analysis
imagery_data<-import_moist("imagery_data_all.csv")
field_data=read.csv("field_moisture_data.csv")
field_data=field_data[1:294, ]
texture_data=read.csv("Texture Calculation/texture_vals.csv")

#get the field data and the imagery data matched up in the same dataframe
df<-make_df(imagery_data,field_data,texture_data)



##check for spatial autocorrelation
##calculate distance matrices for field moisture and x,y coordinates
##check this!!
distxy<-dist(df[,c("X","Y")], method = "euclidean")
distmoist<-dist(df[,c("MoistureTop","MoistureBottom","MoistureLive")], method = "euclidean")

mantel(ydis=distxy, xdis=distmoist, method="pearson", permutations=99999, na.rm=TRUE)




##absent top or live bags cause a problem with NA values when calculating totals
df<-mutate(df, MoistureLiveNoNA = case_when(
        is.na(MoistureLive) == TRUE ~ 0,
        is.na(MoistureLive) == FALSE ~ MoistureLive
        )
```

```
  )
df<-mutate(df, WeightLiveNoNA = case_when(
        is.na(WeightLive) == TRUE ~ 0,
        is.na(WeightLive) == FALSE ~ WeightLive
        )
)
df<-mutate(df, MoistureTopNoNA = case_when(
        is.na(MoistureTop) == TRUE ~ 0,
        is.na(MoistureTop) == FALSE ~ MoistureTop
        )
)
df<-mutate(df, WeightTopNoNA = case_when(
        is.na(WeightTop) == TRUE ~ 0,
        is.na(WeightTop) == FALSE ~ WeightTop
        )
)


##calculate total moisture
df<-mutate(df,TotalMoisture=(MoistureTopNoNA*WeightTopNoNA+MoistureBottom*WeightBottom+MoistureLiveNoNA*WeightLiveNoNA)/(WeightTopNoNA+WeightBottom+WeightLiveNoNA))

##calculate total weight
df<-mutate(df,TotalWeight=WeightTopNoNA+WeightBottom+WeightLiveNoNA)


##make a column for moisture that is total for short grass and top for tall grass
df<-mutate(df,typeMoisture=TotalMoisture)
for (n in 1:60){
```

```
  df[n,"typeMoisture"]=df[n,"MoistureTop"]
}

##make a column for moisture that is total-live
df<-
mutate(df,TotalMoisture_nolive=(MoistureTopNoNA*WeightTopNoNA+MoistureBottom*Wei
ghtBottom)/(WeightTopNoNA+WeightBottom))

##make a column for moisture that is top+live
df<-
mutate(df,typeMoisture_live=(MoistureTopNoNA*WeightTopNoNA+MoistureLiveNoNA*Wei
ghtLiveNoNA)/(WeightTopNoNA+WeightLiveNoNA))



##remove bad data
df$typeMoisture[54]=NA
df$TotalMoisture[54]=NA
df$TotalMoisture_nolive[54]=NA
df$typeMoisture_live[54]=NA

##this one is entirely a bush
df$typeMoisture[8]=NA
df$TotalMoisture[8]=NA
df$TotalMoisture_nolive[8]=NA
df$typeMoisture_live[8]=NA



##try some ratios
df<-mutate(df,NDWI=(NIR-SWIR)/(NIR+SWIR))
df<-mutate(df,NDVI=(NIR-R)/(NIR+R))
df<-mutate(df,VARI=(G-R)/(G+R-B))
```

```
df<-mutate(df,NDGR=(G-R)/(G+R))


##df<-mutate(df,MoistureTransformed=log10(TotalMoisture))


##some plots of moisture distribution
##a little look at variation in moisture
morning <- df %>% subset(SamplePeriod==1)
afternoon <- df %>% subset(SamplePeriod==2)


##plot total moisture by sample period
layout(matrix(c(1),1,1))
transparentBlue <- rgb(0, 0, 255, max = 255, alpha = 125, names = "blue50")
transparentRed <- rgb(255, 0, 0, max = 255, alpha = 125, names = "blue50")
hist1<-hist(morning$TotalMoisture,breaks=20)
hist2<-hist(afternoon$TotalMoisture, breaks=30)
plot(hist2,col=transparentRed)
plot(hist1,col=transparentBlue,add=TRUE)



##plot total moisture by grass type
df<-mutate(df,GrassType=as.factor(GrassType))
ggplot(df,
aes(x=TotalMoisture,fill=GrassType))+geom_histogram(position="identity",alpha=.2,bins=50)+
 xlab("Total Moisture (as proportion of dry weight)")+ylab("Count") + theme(text =
element_text(size=16))

##plot top for tall versus total for tall
```

```
layout(matrix(c(1),1,1))
hist1<-hist(tall$TotalMoisture,breaks=30)
hist2<-hist(tall$MoistureTop, breaks=20)
plot(hist2,col=transparentRed, xlim=c(.08,.85))
plot(hist1,col=transparentBlue,add=TRUE)



##check for normality
shapiro.test(df$typeMoisture)
df<-mutate(df,typeMoisture_transformed=log10(df$typeMoisture))

shapiro.test(df$TotalMoisture)
df<-mutate(df,totalMoisture_transformed=log10(df$TotalMoisture))
shapiro.test(df$totalMoisture_transformed)

shapiro.test(df$TotalMoisture_nolive)
df<-mutate(df,totalMoisture_nolive_transformed=log10(df$TotalMoisture_nolive))

shapiro.test(df$typeMoisture_live)
df<-mutate(df,typeMoisture_live_transformed=log10(df$typeMoisture_live))

##exploratory plotting
p1<-ggplot(df, aes(x=NDWI, y=TotalMoisture)) + geom_point()+theme(text =
element_text(size=14))
p2<-ggplot(df, aes(x=VARI, y=TotalMoisture)) + geom_point()
p3<-ggplot(df, aes(x=NDVI, y=TotalMoisture)) + geom_point()
p4<-ggplot(df, aes(x=NDGR, y=TotalMoisture)) + geom_point()
p5<-ggplot(df, aes(x=B, y=TotalMoisture)) + geom_point()
p6<-ggplot(df, aes(x=G, y=TotalMoisture)) + geom_point()
p7<-ggplot(df, aes(x=R, y=TotalMoisture)) + geom_point()
```

```
p8<-ggplot(df, aes(x=NIR, y=TotalMoisture)) + geom_point()
p9<-ggplot(df, aes(x=SWIR, y=TotalMoisture)) + geom_point()

grid.arrange(p1, p2, p3, p4, p5, p6, p7, p8, p9, nrow = 3)



##plot the different moistures v NDVI for tall grass
p1<-ggplot(df[1:60,], aes(x=NDVI, y=TotalMoisture)) + geom_point()+theme(text = element_text(size=16))
p2<-ggplot(df[1:60,], aes(x=NDVI, y=TotalMoisture_nolive)) + geom_point()+theme(text = element_text(size=16))
p3<-ggplot(df[1:60,], aes(x=NDVI, y=typeMoisture)) + geom_point()+theme(text = element_text(size=16))
p4<-ggplot(df[1:60,], aes(x=NDVI, y=typeMoisture_live)) + geom_point()+theme(text = element_text(size=16))

grid.arrange(p1, p2, p3, p4, nrow = 2)

cor(df[1:60,]$TotalMoisture,df[1:60,]$NDVI, use="complete.obs")
cor(df[1:60,]$TotalMoisture_nolive,df[1:60,]$NDVI, use="complete.obs")
cor(df[1:60,]$typeMoisture,df[1:60,]$NDVI, use="complete.obs")
cor(df[1:60,]$typeMoisture_live,df[1:60,]$NDVI, use="complete.obs")

##plot moisture with and without live for short grass
p1<-ggplot(df[61:120,], aes(x=NDVI, y=TotalMoisture)) + geom_point()+theme(text = element_text(size=14))
p2<-ggplot(df[61:120,], aes(x=NDVI, y=TotalMoisture_nolive)) + geom_point()+theme(text = element_text(size=14))

grid.arrange(p1, p2, nrow = 1)
```

```
cor(df[61:120,]$TotalMoisture,df[61:120,]$NDVI, use="complete.obs")
cor(df[61:120,]$TotalMoisture_nolive,df[61:120,]$NDVI, use="complete.obs")

##modeling with indices
fit1 <- lm(TotalMoisture ~  NDVI + TotalWeight, data=df)
fit2 <- lm(TotalMoisture ~  NDWI, data=df)
fit3 <- lm(TotalMoisture ~  VARI, data=df)
fit4 <- lm(TotalMoisture ~  NDGR, data=df)
fit5 <- lm(TotalMoisture ~  NDVI + TotalWeight + GrassType, data=df)
AIC(fit1,fit2,fit3,fit4,fit5)
summary(fit1)
plot(fit1)
summary(fit2)
summary(fit3)
summary(fit5)



##next try PCA
df_wavelengths<-subset(df, select=c(R,G,B,RE,NIR))
scaled_wavelengths <-scale(df_wavelengths)
PCA<-princomp(scaled_wavelengths, cor = FALSE, scores = TRUE)
PCA_coeff=PCA$loadings[,1:4]
library(ggbiplot)
ggbiplot(PCA, choices=c(2,4)) + geom_point() +theme(text = element_text(size=14))


##PCA again, with SWIR
df_wavelengths_SWIR<- df %>% subset(select=c(R,G,B,RE,NIR,SWIR)) %>%
```

```
  filter(SWIR>0)
scaled_wavelengths_SWIR <-scale(df_wavelengths_SWIR)
PCA_swir<-princomp(scaled_wavelengths_SWIR, cor = FALSE, scores = TRUE)
PCA_coeff_swir=PCA_swir$loadings[,1:4]



##try vars from PCA
##make sure to use standardized values
df<-
mutate(df,PC1=PCA_coeff[1,1]*R_r+PCA_coeff[2,1]*G_r+PCA_coeff[3,1]*B_r+PCA_coeff[4,
1]*RE_r+PCA_coeff[5,1]*NIR_r)
df<-
mutate(df,PC2=PCA_coeff[1,2]*R_r+PCA_coeff[2,2]*G_r+PCA_coeff[3,2]*B_r+PCA_coeff[4,
2]*RE_r+PCA_coeff[5,2]*NIR_r)
df<-
mutate(df,PC3=PCA_coeff[1,3]*R_r+PCA_coeff[2,3]*G_r+PCA_coeff[3,3]*B_r+PCA_coeff[4,
3]*RE_r+PCA_coeff[5,3]*NIR_r)
df<-
mutate(df,PC4=PCA_coeff[1,4]*R_r+PCA_coeff[2,4]*G_r+PCA_coeff[3,4]*B_r+PCA_coeff[4,
4]*RE_r+PCA_coeff[5,4]*NIR_r)


##classification tree
library(mvpart)
##try making classes for 0-.1, .1-.2 .2-.3, .3-.4, .4-.5, .6-.7 and .71+
df <- df %>% mutate(class = case_when(TotalMoisture<=.1 ~ 1,
                          TotalMoisture>.1&TotalMoisture<.2 ~ 2,
                          TotalMoisture>.2&TotalMoisture<.3 ~ 3,
                          TotalMoisture>.3&TotalMoisture<.4 ~ 4,
```

```
                        TotalMoisture>.4&TotalMoisture<.5 ~ 5,
                        TotalMoisture>.5&TotalMoisture<.6 ~ 6,
                        TotalMoisture>.6&TotalMoisture<.7 ~ 7,
                        TotalMoisture>.7 ~ 8))
tree<-mvpart(class~PC1+PC2+PC3+PC4, method="class", df, xv="pick", xvmult=100)




fit_PCA<-lm(TotalMoisture~PC2+PC4+TotalWeight, data=df)
summary(fit_PCA)
layout(matrix(c(1,2,3,4),2,2))
plot(fit_PCA)


##pretty plot of best model
predicted<-predict(fit_PCA)
actual <- df %>% subset(is.na(TotalMoisture)==FALSE)
layout(matrix(c(1),1,1))
ggplot(actual,aes(predicted,TotalMoisture, color=GrassType))+geom_point()+
  geom_abline()+xlab("Predicted Moisture")+ylab("Observed Moisture")+theme(text =
element_text(size=14))
##collinearity of predictors
cor_matrix <- cor(df[11:16])


##fit just each type separately? is it worse in the short grass bc the variation is even lower?
tallfit <- lm(TotalMoisture~PC2+PC4+TotalWeight, data=df[1:60,])
summary(tallfit)
```

```
shortfit <- lm(TotalMoisture~PC2+PC4+TotalWeight,data=df[61:120,])
summary(shortfit)
```

WORKS CITED

1. Coen, J.L.; Natasha Stavros, E.; Fites-Kaufman, J.A. Deconstructing the King megafire. *Ecological Applications* 2018, *28*, 1565–1580.
2. Gillett, N.P. Detecting the effect of climate change on Canadian forest fires. *Geophysical Research Letters* 2004, *31*.
3. Heyerdahl, E.K.; Alvarado, E. Influence of Climate and Land Use on Historical Surface Fires in Pine-Oak Forests, Sierra Madre Occidental, Mexico. *Fire and Climatic Change in Temperate Ecosystems of the Western Americas* 196–217.
4. Hammer, R.B.; Radeloff, V.C.; Fried, J.S.; Stewart, S.I. Wildland - urban interface housing growth during the 1990s in California, Oregon, and Washington. *International Journal of Wildland Fire* 2007, *16*, 255.
5. Mell, W.E.; Manzello, S.L.; Maranghides, A.; Butry, D.; Rehm, R.G. The wildland - urban interface fire problem - current approaches and research needs. *International Journal of Wildland Fire* 2010, *19*, 238.
6. Biswell, H. *Prescribed Burning in California Wildlands Vegetation Management*; Univ of California Press, 1999; ISBN 9780520219458.
7. Fernandes, P.M. Empirical Support for the Use of Prescribed Burning as a Fuel Treatment. *Current Forestry Reports* 2015, *1*, 118–127.
8. Crecente-Campo, F.; Pommerening, A.; Rodríguez-Soalleiro, R. Impacts of thinning on structure, growth and risk of crown fire in a Pinus sylvestris L. plantation in northern Spain. *Forest Ecology and Management* 2009, *257*, 1945–1954.

9. Brown, T.J.; Hall, B.L.; Westerling, A.L. The Impact of Twenty-First Century Climate Change on Wildland Fire Danger in the Western United States: An Applications Perspective. *Climatic Change* 2004, *62*, 365–388.
10. Livingston, A.C.; Morgan Varner, J. Fuel Moisture Differences in a Mixed Native and Non-Native Grassland: Implications for Fire Regimes. *Fire Ecology* 2016, *12*, 73–87.
11. Jolly, W.M.; Matt Jolly, W. Sensitivity of a surface fire spread model and associated fire behaviour fuel models to changes in live fuel moisture. *International Journal of Wildland Fire* 2007, *16*, 503.
12. Chuvieco, E.; Aguado, I.; Dimitrakopoulos, A.P. Conversion of fuel moisture content values to ignition potential for integrated fire danger assessment. *Canadian Journal of Forest Research* 2004, *34*, 2284–2293.
13. Anderson, S.A.J.; Anderson, W.R. Ignition and fire spread thresholds in gorse (Ulex europaeus). *International Journal of Wildland Fire* 2010, *19*, 589.
14. Maki, M.; Ishiahra, M.; Tamura, M. Estimation of leaf water status to monitor the risk of forest fires by using remotely sensed data. *Remote Sensing of Environment* 2004, *90*, 441–450.
15. Schowengerdt, R.A. *Remote Sensing: Models and Methods for Image Processing*; Elsevier, 2012; ISBN 9780080516103.
16. Torresan, C.; Berton, A.; Carotenuto, F.; Di Gennaro, S.F.; Gioli, B.; Matese, A.; Miglietta, F.; Vagnoli, C.; Zaldei, A.; Wallace, L. Forestry applications of UAVs in Europe: a review. *International Journal of Remote Sensing* 2017, *38*, 2427–2447.
17. Banu, T.P.; Borlea, G.F.; Banu, C. The Use of Drones in Forestry. *Journal of Environmental Science and Engineering B* 2016, *5*.

18. Rothermel, R.C. *A Mathematical Model for Predicting Fire Spread in Wildland Fuels*; 1972;

19. Balbi, J.H.; Morandini, F.; Silvani, X.; Filippi, J.B.; Rinieri, F. A physical model for wildland fires. *Combust. Flame* **2009**, *156*, 2217–2230.

20. Mell, W.; Jenkins, M.A.; Gould, J.; Cheney, P. A physics-based approach to modelling grassland fires. *International Journal of Wildland Fire* 2007, *16*, 1.

21. Knipling, E.B. Physical and physiological basis for the reflectance of visible and near-infrared radiation from vegetation. *Remote Sensing of Environment* 1970, *1*, 155–159.

22. Elachi, C.; van Zyl, J. Introduction to the Physics and Techniques of Remote Sensing 2006.

23. Marino, E.; Yebra, M.; Guillén-Climent, M.; Algeet, N.; Tomé, J.L.; Madrigal, J.; Guijarro, M.; Hernando, C. Investigating Live Fuel Moisture Content Estimation in Fire-Prone Shrubland from Remote Sensing Using Empirical Modelling and RTM Simulations. *Remote Sensing* 2020, *12*, 2251.

24. Stow, D.; Niphadkar, M.; Kaiser, J. Time series of chaparral live fuel moisture maps derived from MODIS satellite data. *International Journal of Wildland Fire* 2006, *15*, 347.

25. Hao, X.; Qu, J. Retrieval of real-time live fuel moisture content using MODIS measurements. *Remote Sensing of Environment* 2007, *108*, 130–137.

26. Chuvieco, E.; Riaño, D.; Aguado, I.; Cocero, D. Estimation of fuel moisture content from multitemporal analysis of Landsat Thematic Mapper reflectance data: Applications in fire danger assessment. *International Journal of Remote Sensing* 2002, *23*, 2145–2162.

27. Yebra, M.; Dennison, P.E.; Chuvieco, E.; Riaño, D.; Zylstra, P.; Raymond Hunt, E.; Mark Danson, F.; Qi, Y.; Jurdao, S. A global review of remote sensing of live fuel moisture

content for fire danger assessment: Moving towards operational products. *Remote Sensing of Environment* 2013, *136*, 455–468.

28. Danson, F.M.; Bowyer, P. Estimating live fuel moisture content from remotely sensed reflectance. *Remote Sensing of Environment* 2004, *92*, 309–321.
29. Yebra, M.; Chuvieco, E.; Riaño, D. Estimation of live fuel moisture content from MODIS images for fire risk assessment. *Agricultural and Forest Meteorology* 2008, *148*, 523–536.
30. Dennison, P.E.; Roberts, D.A.; Peterson, S.H.; Rechel, J. Use of Normalized Difference Water Index for monitoring live fuel moisture. *International Journal of Remote Sensing* 2005, *26*, 1035–1042.
31. Peterson, S.; Roberts, D.; Dennison, P. Mapping live fuel moisture with MODIS data: A multiple regression approach. *Remote Sensing of Environment* 2008, *112*, 4272–4284.
32. Stow, D.; Niphadkar, M. Stability, normalization and accuracy of MODIS□derived estimates of live fuel moisture for southern California chaparral. *International Journal of Remote Sensing* 2007, *28*, 5175–5182.
33. Finney, M.A. FARSITE: Fire Area Simulator-model development and evaluation 1998.
34. Agee, J.K.; Wright, C.S.; Williamson, N.; Huff, M.H. Foliar moisture content of Pacific Northwest vegetation and its relation to wildland fire behavior. *Forest Ecology and Management* 2002, *167*, 57–66.
35. McGrattan, K.B.; McDermott, R.; Weinschenk, C.; Overholt, K.; Hostikka, S.; Floyd, J. Fire dynamics simulator technical reference guide volume 1 : 2013.
36. Mell, W.; McNamara, D.; Maranghides, A.; McDermott, R.; Forney, G.; Hoffman, C.; Ginder, M. Computer modelling of wildland-urban interface fires. *Fire & Materials* **2011**.

37. Hudak, A.T.; Kato, A.; Bright, B.C.; Louise Loudermilk, E.; Hawley, C.; Restaino, J.C.; Ottmar, R.D.; Prata, G.A.; Cabo, C.; Prichard, S.J.; et al. Towards Spatially Explicit Quantification of Pre- and Postfire Fuels and Fuel Consumption from Traditional and Point Cloud Measurements. *Forest Science* 2020, *66*, 428–442.

38. Haase, S.M.; Sánchez, J.; Weise, D.R. Evaluation of standard methods for collecting and processing fuel moisture samples 2016.

39. Wang, L.; Raymond Hunt, E.; Qu, J.J.; Hao, X.; Daughtry, C.S.T. Remote sensing of fuel moisture content from ratios of narrow-band vegetation water and dry-matter indices. *Remote Sensing of Environment* 2013, *129*, 103–110.

40. Asner, G.P. Biophysical and Biochemical Sources of Variability in Canopy Reflectance. *Remote Sensing of Environment* 1998, *64*, 234–253.

41. Stark, B.; McGee, M.; Chen, Y. Short wave infrared (SWIR) imaging systems using small Unmanned Aerial Systems (sUAS). *2015 International Conference on Unmanned Aircraft Systems (ICUAS)* 2015.

42. Viljanen, N.; Honkavaara, E.; Näsi, R.; Hakala, T.; Niemeläinen, O.; Kaivosoja, J. A Novel Machine Learning Method for Estimating Biomass of Grass Swards Using a Photogrammetric Canopy Height Model, Images and Vegetation Indices Captured by a Drone. *Agriculture* 2018, *8*, 70.

43. Tucker, C.J. Remote sensing of leaf water content in the near infrared. *Remote Sensing of Environment* 1980, *10*, 23–32.

44. Huete, A.R. A soil-adjusted vegetation index (SAVI). *Remote Sensing of Environment* 1988, *25*, 295–309.

45. Gao, B.-C. NDWI—A normalized difference water index for remote sensing of vegetation liquid water from space. *Remote Sensing of Environment* 1996, *58*, 257–266.

46. Rowlands, A. *Physics of Digital Photography*; 2017; ISBN 9780750312431.

47. Sandino, J.; Gonzalez, F.; Mengersen, K.; Gaston, K.J. UAVs and Machine Learning Revolutionising Invasive Grass and Vegetation Surveys in Remote Arid Lands. *Sensors* **2018**, *18*, doi:10.3390/s18020605.

48. Xiang, H.; Tian, L. Development of a low-cost agricultural remote sensing system based on an autonomous unmanned aerial vehicle (UAV). *Biosystems Engineering* 2011, *108*, 174–190.

49. Hardisky MA, E. al The influence of soil salinity, growth form, and leaf moisture on the spectral radiance of Spartina Alterniflora Canopies. *Photogrammetric Engineering and Remote Sensing* **1983**.

50. Hardy CC, E. al Evaluation of NDVI for monitoring live moisture in three vegetation types of the western US. *Photogrammetric Engineering and Remote Sensing* **1999**.

51. Jenal, A.; Bareth, G.; Bolten, A.; Kneer, C.; Weber, I.; Bongartz, J. Development of a VNIR/SWIR multispectral imaging system for vegetation monitoring with unmanned aerial vehicles. *Sensors (Basel)* **2019**, *19*, doi:10.3390/s19245507.

52. Gruszczyński, W.; Puniach, E.; Ćwiąkała, P.; Matwij, W. Application of convolutional neural networks for low vegetation filtering from data acquired by UAVs. *ISPRS J. Photogramm. Remote Sens.* **2019**, *158*, 1–10.

53. Manly, B.F.J.; Navarro Alberto, J.A. *Multivariate Statistical Methods: A Primer, Fourth Edition*; CRC Press, 2016; ISBN 9781498728997.

54. Caccamo, G.; Chisholm, L.A.; Bradstock, R.A.; Puotinen, M.L.; Pippen, B.G. Monitoring live fuel moisture content of heathland, shrubland and sclerophyll forest in south-eastern Australia using MODIS data. *Int. J. Wildland Fire* **2012**, *21*, 257.
55. Hardy, C.C.; Burgan, R.E. Evaluation of NDVI for monitoring live moisture in three vegetation types of the western US. *Photogramm. Eng. Remote Sens.* **1999**, *65*, 603–610.
56. Lim, J.; Watanabe, N.; Yoshitoshi, R.; Kawamura, K. Simple in□field evaluation of moisture content in curing forage using normalized differece vegetation index (NDVI). *Grassl. Sci.* **2020**, *66*, 238–248.
57. Elachi, C.; Zimmerman, P.D. Introduction to the physics and techniques of remote sensing. *Phys. Today* **1988**, *41*, 126–126.
58. Qi, J.; Chehbouni, A.; Huete, A.R.; Kerr, Y.H.; Sorooshian, S. A modified soil adjusted vegetation index. *Remote Sens. Environ.* **1994**, *48*, 119–126.
59. White, J.C.; Coops, N.C.; Wulder, M.A.; Vastaranta, M.; Hilker, T.; Tompalski, P. Remote sensing technologies for enhancing forest inventories: A review. *Can. J. Remote Sens./J. Can. Teledetect.* **2016**, *42*, 619–641.
60. Näsi, R.; Viljanen, N.; Kaivosoja, J.; Alhonoja, K.; Hakala, T.; Markelin, L.; Honkavaara, E. Estimating biomass and nitrogen amount of barley and grass using UAV and aircraft based spectral and photogrammetric 3D features. *Remote Sens. (Basel)* **2018**, *10*, 1082.
61. Walter, J.; Edwards, J.; McDonald, G.; Kuchel, H. Photogrammetry for the estimation of wheat biomass and harvest index. *Field Crops Res.* **2018**, *216*, 165–174.